Acta Materialia 258 (2023) 119237

Contents lists available at ScienceDirect

Acta Materialia

journal homepage: www.elsevier.com/locate/actamat

Full length article

Revealing shear-coupled migration mechanism of a mixed tilt-twist grain boundary at atomic scale

Zhengwu Fang [a], Boyang Li [a], Susheng Tan [b], Scott Mao [a], Guofeng Wang [a,*]

[a] Department of Mechanical Engineering and Materials Science, University of Pittsburgh, Pittsburgh, PA 15261, USA
[b] Petersen Institute of Nanoscience and Engineering, University of Pittsburgh, Pittsburgh, Pennsylvania 15260, USA

ARTICLE INFO

Keywords:
Grain boundary migration
Mixed tilt-twist grain boundary
Grain boundary plane
Grain boundary sliding

ABSTRACT

Shear-coupled grain boundary (GB) migration greatly influences the plasticity and creep resistance of nanocrystalline materials. However, the atomistic mechanisms underlying the shear-coupled migration of general mixed tilt-twist GBs (MGBs) remain largely elusive to date. Here, using in-situ high-resolution transmission electron microscopy and molecular dynamics simulations, we uncover the atomic-scale migration behavior of a typical MGB, i.e., $\langle 001\rangle\{200\}/\langle 0\bar{1}1\rangle\{\bar{1}11\}$ GB, during the room-temperature shear deformation of Au nanobicrystals. Two distinct migration patterns showing the opposite signs of shear-coupling factor were observed and further revealed to be mediated by the motion of GB disconnections with different crystallographic parameters and exhibit different lattice correspondence relations, i.e., $\langle 001\rangle\{020\}$-to-$\langle 0\bar{1}1\rangle\{200\}$ and $\langle 001\rangle\{020\}$-to-$\langle 0\bar{1}1\rangle\{111\}$. Simulation results confirm that the two distinct migration patterns could be activated under different stress/strain states. Moreover, excess GB sliding and GB plane reorientation were found to accommodate the GB migration in both experiments and simulations, likely due to the necessity of establishing a point-to-point lattice correspondence during GB migration. These findings provide atomic-scale experimental evidence on the disconnection-mediated migration of MGBs and elaborate on the hitherto unreported complex shear response of MGBs, which have valuable implications for optimizing the ductility of metallic nanocrystals through controlling GB migration.

1. Introduction

Stress-induced grain boundary (GB) migration plays a critical role in the plastic deformation and microstructural evolution of nanocrystalline materials [1–3]. Promoting GB migration at room temperature can significantly improve the ductility of nanocrystalline materials [4], while inhibiting GB migration at high temperature could largely enhance the creep resistance of nanocrystals [5]. Understanding the mechanisms of GB migration, especially at the atomic scale, provides important guidelines for tailoring the mechanical properties of nanocrystalline materials through GB engineering. Previous studies reveal that stress-induced GB migration is usually coupled to shear deformation (or GB sliding), namely shear-coupled GB migration [6,7]. The shear-coupling factor [3,6], as defined by $\beta = s/m$ where s is the magnitude of GB sliding and m is the distance of GB migration, is used to characterize the GB migration.

Numerous experimental [3,8-12], simulation [6,13,14], and theoretical studies [15–17] have been conducted to investigate the shear-coupled GB migration behavior in face-centered cubic metals, with the main focus on simple tilt GBs. Despite that the GBs in these metals are generally mixed tilt-twist GBs (MGBs) [18], the shear-coupled migration behavior of general MGBs has not been fully described and the atomistic mechanisms of the shear-coupled migration of MGB remain largely elusive to date. One micro-scale experimental study revealed the concurrent GB migration and grain rotation during the shear-coupled migration of an MGB in an aluminum bicrystal, where it was deduced that only the tilt component of the MGB determines its shear-coupling factor [19]. Recently, a disconnection model was proposed to describe the GB migration [20]. For high-symmetry GBs such as Σ11(113) symmetrical tilt GB and Σ5(210) symmetrical tilt GB, the simply disconnection-mediated GB migration has been evidenced in both experiments [12,21,22] and simulations [23–26]. In comparison, low-symmetry GBs such as the asymmetrical tilt GB and the MGB may show some special deformation behavior other than the

* Corresponding author.
E-mail address: guw8@pitt.edu (G. Wang).

https://doi.org/10.1016/j.actamat.2023.119237
Received 30 December 2022; Received in revised form 15 June 2023; Accepted 8 August 2023
Available online 9 August 2023

disconnection-mediated GB migration, such as GB sliding [27], GB facet transformation [14,28,29], and GB dissociation [14,28,29]. Although simulations [30] suggest that thermal-driven migration of some MGBs could be mediated by the motion of step or kink flows, i.e., arrays of disconnections, experimental evidence on whether or how the shear-coupled migration of MGBs is mediated by the GB disconnection is still missing.

In this work, by performing in-situ high-resolution transmission electron microscope (HRTEM) mechanical testing combined with molecular dynamics (MD) simulations, we investigate the shear-coupled migration behavior of a typical MGB, i.e., $\langle 001\rangle\{200\}/\langle 0\bar{1}1\rangle\{\bar{1}11\}$ GB, during the room-temperature shear deformation of custom-fabricated Au nanocrystals. Atomic-scale experimental evidence that the shear-coupled migration of MGBs is mediated by GB disconnections is presented. Compared to the migration of symmetrical tilt GBs mediated by a single type of GB disconnection [12,14], the $\langle 001\rangle\{200\}/\langle 0\bar{1}1\rangle\{\bar{1}11\}$ MGB shows two distinct migration patterns that exhibit the opposite signs of shear-coupling factors and different lattice correspondence relations, which are attributed to the activation of GB disconnections with different Burgers vectors. Moreover, the shear-coupled migration of the MGB is cooperated by GB plane reorientation and excess GB sliding occurring at the identical MGB plane, as to establish a point-to-point lattice correspondence during GB migration. Consequently, our findings unprecedently reveal the underlying atomistic mechanisms of the shear-coupled migration of MGBs and the complex mechanical response of MGBs under shear loading, which offer important guidance towards developing metallic nanocrystalline materials with superior mechanical properties via controlling GB migration.

2. Experimental and simulation methods

2.1. In-situ nanowelding and shear testing

In-situ nanowelding and shear testing were conducted inside an FEI Titan Themis G2 200 probe Cs-corrected scanning transmission electron microscope (STEM) using a Nanofactory scanning tunneling microscope (STM) holder. High-purity (99.999%) Au wires (from ESPI metals) with diameter of 0.254 mm were used to fabricate Au nano-bicrystals. First, the Au wires were cut into rods with a length of ~5 mm in order to be properly loaded onto the sample side and the probe side of the STM holder (Supplementary Fig. 1a and 1b). Then, one end of the Au rod loaded onto the sample side was torn apart with a wire cutter to create the fracture surface with plentiful nanotips (Supplementary Fig. 1c); one end of the Au rod loaded onto the probe side was cut into a wedge shape with a wire cutter. The STM holder along with the loaded samples was plasma cleaned in a Tergeo-EM plasma cleaner (PIE Scientific) before inserted into the microscope. These preparation procedures ensure that the nanotips are sufficiently clean for subsequent sample fabrication (Supplementary Fig. 1d). To fabricate the bicrystals with MGBs, sharp nanotips of Au with the zone axes of $\langle 110\rangle$ and $\langle 100\rangle$ were selected to be welded together by controlling the movement of the probe side and applying a constant voltage of ~2 V on the probe side. All in-situ shear tests were conducted by moving the probe side with the piezo-manipulator of the STM holder at a constant rate of between 0.001 and 0.01 nm s^{-1}. The images were observed in HRTEM mode and recorded in real-time by a charge-coupled device camera at a frame rate of 0.25 s per frame. All in-situ experiments were performed under low-dose beam conditions to minimize the potential beam effects on GB migration behaviors.

2.2. Molecular dynamics simulations

Molecular dynamics (MD) simulations were performed using the Large-scale Atomic/Molecular Massively Parallel Simulation (LAMMPS) code [31] and an embedded atom method (EAM) potential [32] for Au. A total of three Au bicrystal models that were constructed by joining two separate crystal lattices (grain 1 and grain 2 in Fig. 1a) with different lattice orientations (as shown in Fig. 1b-1d) together along the Z axis are studied in this work. The Au bicrystals with the lattice orientations as shown in Fig. 1b and 1c (denoted as model 1 and model 2) were constructed to verify the two admissible lattice correspondence relations during the migration of the $\langle 001\rangle\{200\}/\langle 0\bar{1}1\rangle\{\bar{1}11\}$ GB, whereas the bicrystal with the lattice orientations in Fig. 1d (denoted as model 3) was used to examine the purely shear-coupled GB migration when the GB plane has an inclination angle of ~19° to the $\langle 001\rangle\{200\}/\langle 0\bar{1}1\rangle\{\bar{1}11\}$ GB.

Structural optimization of these bicrystals was performed using the conjugate gradient method and with periodic boundary conditions along all three dimensions. Note that the lattices in all bicrystal models are slightly strained to meet the periodic boundary conditions given that the periods of the lattices in directions parallel to the GB planes, i.e., X and Y axes, are incommensurate. The applied strains and the dimensions of these bicrystals are summarized in Supplementary Table 1. This is a commonly used strategy to construct the incommensurate GBs in simulations [33–35]. We have also examined different integer ratios of the period to construct the bicrystals (i.e., different strains and dimensions), and the observed shear-coupled GB migration behavior is quite similar. The bicrystal models were further equilibrated at 300 K with a pressure of 0 bar for 50 ps using the isobaric-isothermal (NPT) ensemble MD simulations. Two thin slabs with a thickness of 1 nm at the top and the bottom of the bicrystals were fixed, and the shear deformation was applied by displacing the top fixed slabs moving along the X axis of the bicrystals at a constant speed of 1 m s^{-1} (Fig. 1a). The shear deformation of the bicrystals was performed at 300 K via the canonical (NVT) ensemble, with periodic boundary conditions along the Y axis and free surfaces along X and Z axes. The visualization of MD results was performed in OVITO [36]. The common neighbor analysis modifier was used to identity the GB atoms (colored in white) and the atoms in the different crystal structures, i.e., the face-centered cubic, body centered cubic, and hexagonal close-packed crystal structures are colored in green, blue, and red, respectively.

3. Results

3.1. Two distinct types of migration behavior of an identical MGB

Fig. 2a presents the HRTEM image of the as-fabricated Au bicrystal with a diameter of ~14 nm at the neck region. Based on the HRTEM image and corresponding fast Fourier transform (FFT) pattern, it is confirmed that G1 is $\langle 001\rangle$-oriented, G2 is $\langle 0\bar{1}1\rangle$-oriented, and the (200) plane of G1 exactly matches the $(\bar{1}11)$ plane of G2 at the interface. Thus, this interface is identified as $\langle 001\rangle_1\{200\}_1/\langle 0\bar{1}1\rangle_2\{\bar{1}11\}_2$ GB, which is an incommensurate GB due to the irrational ratio of lattice spacing across the interface (i.e., the ratio is $\sqrt{6}/2$). In addition, it is an MGB since the rotation axis for the orientation relationship of this bicrystal is $\langle 0.2443, 0.5898, 0.7689\rangle$ with a rotation angle of ~56.63°. The filtered inverse FFT (IFFT) pattern of the GB region, as inserted at the bottom of Fig. 2a, is obtained by selecting the diffraction spots of $\{020\}_1$ and $\{111\}_2$ (enclosed by the red circles in the inserted FFT pattern). As shown in the filtered IFFT pattern, the GB structure shows the quasi-periodic feature with uniform distribution of GB misfit dislocations at an average distance of ~1.09 nm along the GB. The value of 1.09 nm is close to the ideal structural repeat distance of this GB, which is ~1.11 nm and calculated by $\left[\left|\frac{1}{4}\langle 211\rangle\right| \left|\frac{1}{2}\langle 010\rangle\right|\right]/\left[\left|\frac{1}{4}\langle 211\rangle\right| - \left|\frac{1}{2}\langle 010\rangle\right|\right]$. It should be mentioned that the quasi-periodic feature of GB structure is commonly observed in various types of incommensurate interfaces [37–39].

Interestingly, performing shear tests on the Au bicrystals with the same orientation relationship as that shown in Fig. 2a, we observed two distinct types of shear-coupled migration behavior of this MGB. Fig. 2b-

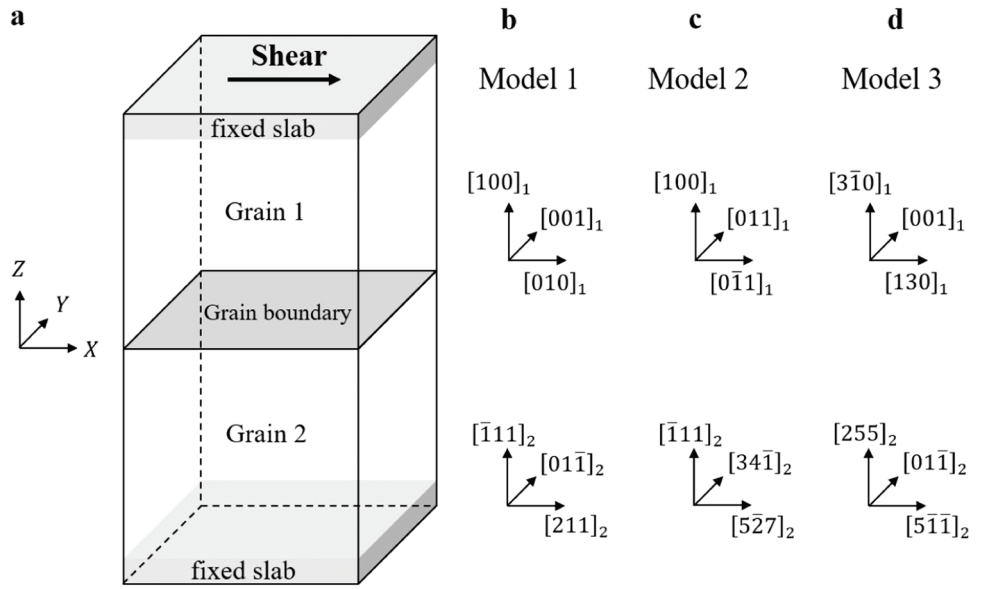

Fig. 1. Schematic (a) and crystallographic orientations (b-d) of the Au bicrystal models used in MD simulations.

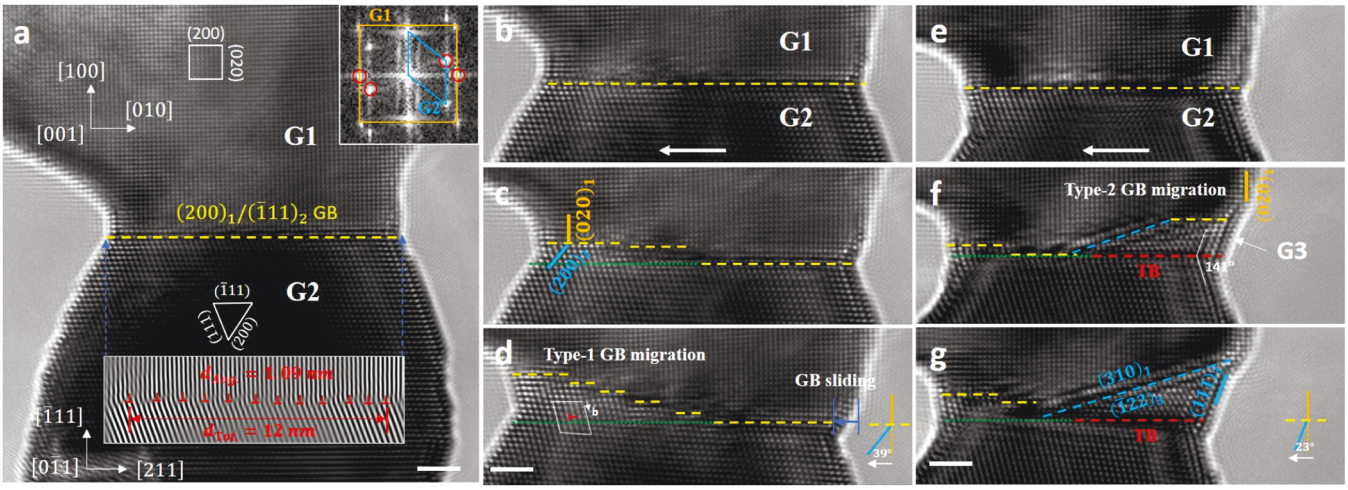

Fig. 2. Two distinct types of shear-coupled migration behavior of the $\langle 001\rangle\{200\}/\langle 0\bar{1}1\rangle\{\bar{1}11\}$ MGB in Au bicrystals. (a) As-fabricated Au bicrystal containing a flat $\{200\}/\{\bar{1}11\}$ MGB at the neck region. Fast Fourier transformation (FFT) pattern and filtered Inversed FFT (IFFT) pattern are inserted to show the crystallography of the bicrystal and the semi-coherent feature of the GB. (b-d) With the applied shear deformation (indicated by the white arrow), part of the GB migrated upwards along the [100] direction of grain 1 (denoted as G1) by transforming the $(200)_1$ plane of G1 into the $\{\bar{1}11\}_2$ plane of grain 2 (denoted as G2). (e-f) With the "same" shear loading, another type of GB migration behavior that also involves the transformation of (200) plane into $\{\bar{1}11\}$ plane was observed. This kind of GB migration is accompanied by the formation of new grain G3 that is in a twinning relationship with G2. Scale bar: 2 nm.

d and 2e-g present the sequential HRTEM snapshots showing the two distinct types of shear-coupled GB migration under the "same" shear loading condition (indicated by the white arrows). It is found that although the GBs in the two cases both migrate towards the [100] direction of G1 and lead to the $[001](200)$-to-$[0\bar{1}1](\bar{1}11)$ plane transformation, one is from G1 into G2 (Fig. 2b-d, denoted as type-1 GB migration as follows) and the other is from G1 into a newly-formed grain G3 (Fig. 2e-g, type-2 GB migration) which is in twinning relationship with G2. Due to the mirror symmetry of the twin boundary, these two types of GB migration migrate towards the same direction under the "opposite" shear loading condition, which indicates the opposite signs of shear-coupling factors. Note that grain G2 rotates slightly by ~3° with the shear strain accumulating, which is likely responsible for the observed lattice distortion and few scattered lattice dislocations in G2 (Fig. 2d and 2g).

Moreover, the shear deformation of the bicrystals was not fully coupled to either type-1 or type-2 GB migration. Specifically, type-1 GB migration as shown in Fig. 2b-d cooperated with the excess GB sliding (indicated by the blue arrow in Fig. 2d) that occurred on the identical $\langle 001\rangle_1\{200\}_1/\langle 0\bar{1}1\rangle_2\{\bar{1}11\}_2$ MGB plane to accommodate the overall shear deformation; while the shear deformation of the bicrystal in Fig. 2e-g was accommodated by the type-2 GB migration along with the upward migration of the residual original MGB (i.e., type-1 GB migration). In addition, GB plane reorientation was observed after both types of GB migration (Fig. 2d and 2g). The above experimental results indicate that the shear-coupled migration of MGBs is more complicated than that of tilt GBs where the GB migration is usually conservative (i.e., GB structure and GB plane nearly keep the same during the migration) and fully coupled to shear deformation [12,40].

3.2. Atomistic processes of the two distinct types of GB migration

To explore the atomistic mechanisms of the type-1 and type-2 GB migration, frame-by-frame analyses on the GB structural evolution during the migration were conducted and shown in Fig. 3a-f and 3 g-l, respectively. It is found that the type-1 GB migration is mainly via the nucleation and motion of GB disconnections with a step height of one atomic layer on the original $\{200\}_1/\{\bar{1}11\}_2$ GB (Fig. 3a-c). The directions of GB disconnection motion and GB migration are along [010] and [100] directions of G1, respectively. The inserts in Fig. 3a and 3b indicate the lattice deformation after the glide of a GB disconnection, which clearly show the displacement of atom columns on the $(\bar{1}11)$ plane of G2 by a maximum value of ~1.4 Å during this process. The GB disconnections with the step height of two or three atomic layers were also observed (Fig. 3d and 3e), which are likely to be formed via the composition of one-layer GB disconnections (Fig. 3c-d) and can decompose back into one-layer disconnections in the subsequent deformation (Fig. 3e-f). Note that the serrated $\{200\}_1$ and $\{020\}_1$ edge surface morphology of G1 is replaced by the $\{111\}_2$ facet after the type-1 GB migration. It is believed that the $\{020\}_1$ planes of G1 are transformed into the $\{200\}_2$ planes of G2 during the GB migration.

In comparison, type-2 GB migration is not via the direct migration of original $\{200\}_1/\{\bar{1}11\}_2$ GB. It is enabled by the formation of a new grain G3 at the incipient stage of deformation (Fig. 3h), which could be a product of GB dissociation [29]. Grain G3 has its $\{\bar{1}11\}$ planes parallel to the $\{200\}$ plane of G1 and is in a twinning relationship with G2. It should be emphasized that the subsequent growth of G3 is not via twinning (i.e., the glide of twinning partials on the twin boundary) but via the migration of GBs between G1 and G3 (Fig. 3i-j), including an inclined GB (roughly the $\{3\bar{1}0\}_1/\{\bar{1}22\}_3$ GB) and the horizontal $\{200\}_1/\{\bar{1}11\}_3$ GB. Here, we focus on the migration of $\{200\}_1/\{\bar{1}11\}_3$ GB facet to make the direct comparison to type-1 GB migration. One-layer GB disconnections are also observed to mediate the migration of this GB (Fig. 3j and 3k). However, different from the process of type-1 GB migration, the motion of these GB disconnections appears to transform the $\{020\}_1$ planes into the $\{111\}_3$ planes, as evidenced by the clockwise rotation of the surface facet by an angle of ~23°.

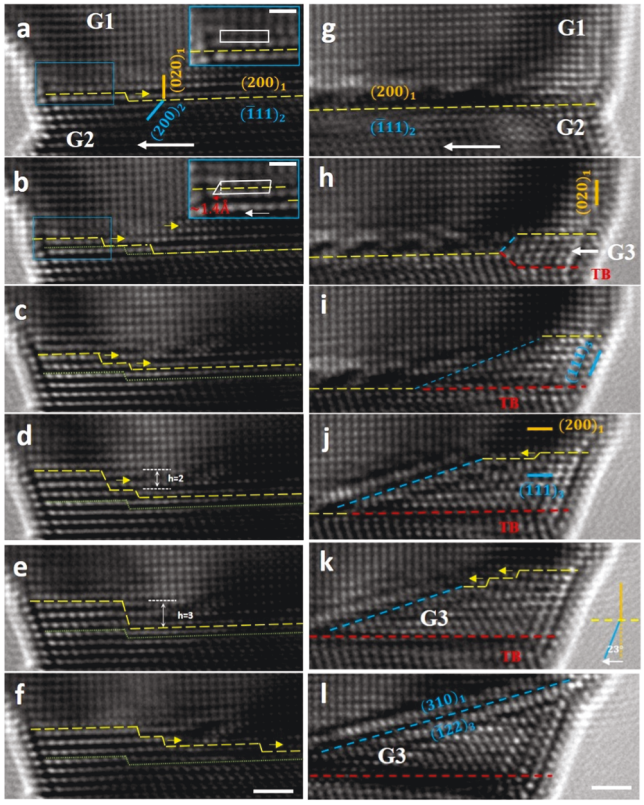

Fig. 3. Sequential HRTEM snapshots showing the atomistic processes of the two types of GB migration behavior. (a-f) Type-1 GB migration via the continuous motion of GB steps/disconnections. These disconnections are primarily at the step height of the one-atomic layer, but the formation and decomposition of disconnections with a step height of two or three atomic-layer were also observed. Inserts in (a) and (b) show the lattice deformation during GB migration, indicating the transformation from $(020)_1$ plane into $(200)_2$ plane during the process. (g-l) Type-2 GB migration that was accompanied by the formation and growth of a new grain (denoted as G3). The growth of G3 was via the migration of GBs between G1 and G3 (indicated by the blue and the yellow dash lines). Some GB disconnections with the step height of one atomic layer can be identified on the $\{200\}_1/\{\bar{1}11\}_3$ GB. Scale bar: (a-l), 1 nm; inserts in (a,b), 0.5 nm.

3.3. Theoretical analysis of the GB disconnections

To elucidate the above experimental results that the two types of GB migration can both be mediated by the motion of one-layer GB disconnections, we conducted theoretical analysis of the crystallographic parameters of these GB disconnections. By comparing the GB disconnections as shown in Fig. 4a, it is found that the two disconnections migrate towards the same direction under the "opposite" shear loading (Fig 4a_2 is flipped horizontally for direct comparison). It is thus inferred that the Burgers vectors of these disconnections are in opposite directions. According to the Pond topological theory of bicrystallography [41,42], the Burgers vectors of interfacial defects can be determined by carrying out the Volterra operation at the incompatible surface steps constructing the interfacial defects (Fig. 4b), which gives

$$\boldsymbol{b} = \boldsymbol{t}(\lambda) - \boldsymbol{P}\boldsymbol{t}(\mu) \quad (1)$$

Where $\boldsymbol{t}(\lambda)$ and $\boldsymbol{t}(\mu)$ are translation vectors defining the surface steps on the adjacent crystals (Fig. 4b), **P** is a transformation matrix re-expressing $\boldsymbol{t}(\mu)$ in the coordinate frame of λ. Because the $\langle 001\rangle_1\{200\}_1/\langle 0\bar{1}1\rangle_2\{\bar{1}11\}_2$ GB exhibits semi-coherent feature (Fig. 2a), the strained coherent dichromatic pattern (CDP) was used as the reference to analyze the Burgers vectors of disconnections [43]. The CDP could be obtained by applying biaxial strains to the two half-crystals in order to bring them into coherency at the interface. Here, the two half-crystals were equally strained to form the coherent reference state indicated by the dark unfilled symbols in Fig. 4c. A unit cell of the coherent reference state at the interface is marked by the dark solid lines in Fig. 4c, which shows the planar spacings along the two commensurate directions, i.e., $[001]_1$ and $[010]_1$, equal to $(\sqrt{6}+2)a/8$ and $(\sqrt{2}+2)a/8$, respectively. Accordingly, the coherent dichromatic pattern (CDP) for the analysis of disconnections of the $\langle 001\rangle\{200\}/\langle 0\bar{1}1\rangle\{\bar{1}11\}$ GB can be obtained as shown in Fig. 4d, where μ is the $\langle 001\rangle$-oriented G1 indicated by symbols in dark blue and λ is the $\langle 0\bar{1}1\rangle$-oriented G2 represented in light blue. The square and circle symbols indicate the atoms belonging to different $\{002\}_1$ or $\{0\bar{1}1\}_2$ planes along the out-of-paper direction. As shown in Fig. 4d, for the translation vector $\boldsymbol{t}(\mu) = \frac{1}{2}\langle\bar{1}01\rangle_1$for the $\langle 001\rangle$-oriented G1, there are two types of admissible translation vector $\boldsymbol{t}(\lambda)$, i.e., $\frac{1}{4}\langle 2\bar{1}\bar{1}\rangle_2$ or $\frac{1}{2}\langle 011\rangle$, for the $\langle 0\bar{1}1\rangle$-oriented G2. Consequently, there are two different combinations of translation vectors to construct the one-layer disconnections, which would generate two different Burgers vectors (numbered as $\boldsymbol{b}_1$ and $\boldsymbol{b}_2$, Fig. 4d). Crystallographic parameters of these two admissible Burgers vectors are listed in Table 1. It is shown that $\boldsymbol{b}_1$ and $\boldsymbol{b}_2$ disconnections both contain the Burgers vector components perpendicular to the GB plane (denoted as $\boldsymbol{b}_p$), which is small ($|\boldsymbol{b}_p| = \frac{2\sqrt{3}-3}{6}a$, $a = 4.08$ Å is the lattice constant of Au) and should be efficiently accommodated by the disconnections themselves [44]. Moreover, $\boldsymbol{b}_1$ type disconnection has an edge component $\boldsymbol{b}_e$ ($|\boldsymbol{b}_e| = \frac{\sqrt{6}+2}{12}a$) and

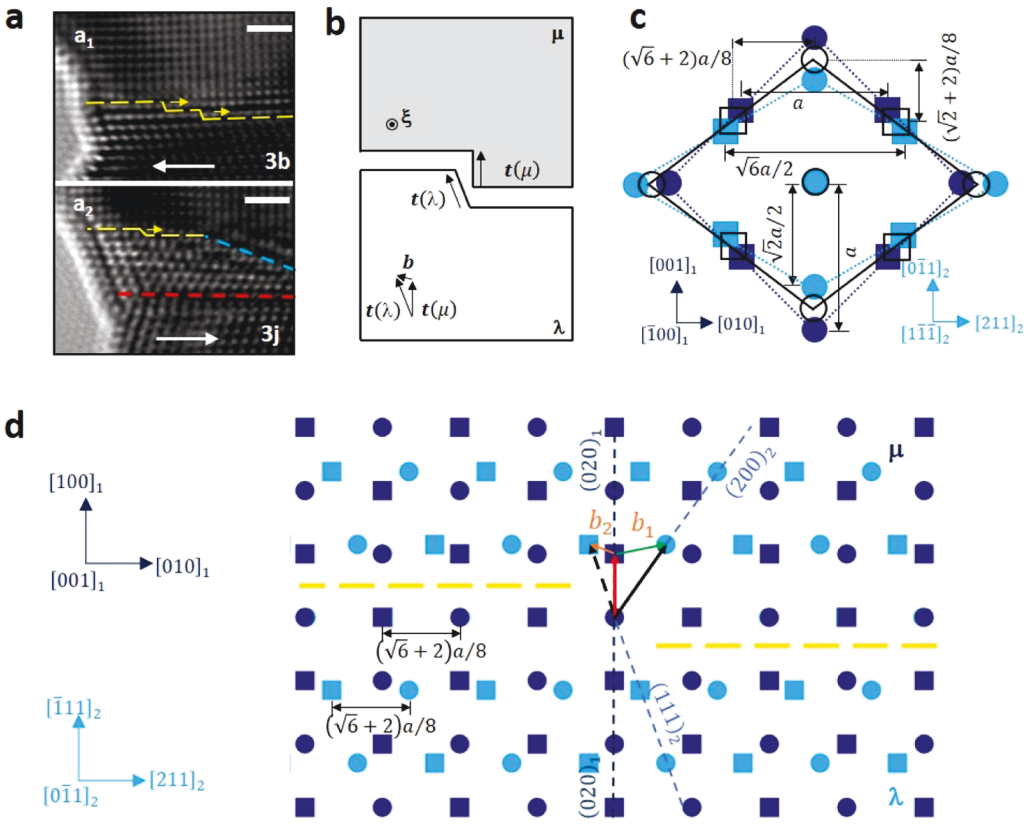

Fig. 4. Theoretical analysis of admissible GB disconnections of ⟨001⟩{200}/⟨0$\bar{1}$1⟩{$\bar{1}$11} MGB. (a) Comparison of the GB disconnections mediating the two types of GB migration. (a_1) is cropped from Fig. 3b whereas (a_2) is taken from Fig. 3j and reoriented for comparison. (b) Schematic illustration showing the formation of a GB disconnection by bonding the two incompatible surface steps. The direction of the sense vector ξ is out-of-paper. (c) Schematic illustration showing the construction of a strained coherent reference state at the GB plane. The dark blue, light blue, and dark unfilled symbols indicate the unstrained (200) plane of crystal μ, the unstrained ($\bar{1}$11) plane of crystal λ, and the coherent reference state, respectively. The cubic and circle symbols indicate the atoms in different depths along the $[001]_1$ direction. (d) Coherent dichromatic pattern for the disconnection analysis of ⟨001⟩{200}/⟨0$\bar{1}$1⟩{$\bar{1}$11} GB. The dark blue and light blue symbols in (d) indicate the strained crystal μ and crystal λ, separately. The yellow dash lines make the GB plane with a disconnection on it.

Table 1
Crystallographic parameters of two admissible one-layer disconnections. $\boldsymbol{b}_e$ and $\boldsymbol{b}_s$ represent the Burgers vectors of their edge and screw components, and $\boldsymbol{b}_p$ indicates the Burgers vector component that is perpendicular to the GB plane.

Disconnection type	$t(\lambda)$	$t(\mu)$	$\boldsymbol{b}_e$	$\boldsymbol{b}_p$	$\boldsymbol{b}_s$
$\boldsymbol{b}_1$	$\frac{1}{2}<011>$	$\frac{1}{2}<\bar{1}01>$	$\frac{\sqrt{6}+2}{12}a$	$\frac{2\sqrt{3}-3}{6}a$	$\frac{\sqrt{2}+2}{8}a$
$\boldsymbol{b}_2$	$\frac{1}{4}<2\bar{1}\bar{1}>$	$\frac{1}{2}<\bar{1}01>$	$\frac{\sqrt{6}+2}{24}a$	$\frac{2\sqrt{3}-3}{6}a$	0

a screw component $\boldsymbol{b}_s$ ($|\boldsymbol{b}_s| = \frac{2+\sqrt{2}}{8}a$). In contrast, $\boldsymbol{b}_2$ type disconnection has only the edge component $\boldsymbol{b}_e$ ($|\boldsymbol{b}_e| = \frac{\sqrt{6}+2}{24}a$). In addition, the edge component of $\boldsymbol{b}_1$ is in the opposite direction of that of $\boldsymbol{b}_2$. It should be mentioned that the crystallographic parameters of these two admissible types of disconnections (Table 1) are deduced on the basis of a strained CDP which is a purely topological model. In addition, non-affine movement of atoms (i.e., shuffling) is believed to be indispensable to accomplish the GB migration. Therefore, it is hard to determine the exact values of the Burgers vectors of these disconnections at this point. Referring to the right-hand rule of determining the motion direction of a given dislocation under an applied shear stress, we find that the motion of $\boldsymbol{b}_1$ type disconnections would mediate the type-1 GB migration (Fig. 3a-f) whereas the $\boldsymbol{b}_2$ type disconnections accommodate the type-2 GB migration (Fig. 3g-l). One further evidence is that the maximum lattice displacement generated by the glide of disconnection during type-1 GB migration is ~1.4 Å (as measured in the inserts of Fig. 3a-b), which reseaonably matches the magnitude of the edge component of $\boldsymbol{b}_1$ disconnection.

Furthermore, one may find from Fig. 4d that the two types of GB migration lead to different lattice correspondence relationships during GB migration as the movement of atoms is along different directions. In both cases, $(200)_1$ atomic plane would transform into $(\bar{1}11)_2$ atomic plane during disconnection-mediated GB migration as the two planes are parallel to the GB. This transformation process involves in-plane atom shuffling as shown in Fig. 5b. However, for the other atomic planes that are not parallel to the GB, lattice correspondence relationships of the two types of GB migration are different. Specifically, the type-1 GB migration mediated by the $\boldsymbol{b}_1$ type disconnection would transform the $(020)_1$ plane of G1 into the $(200)_2$ plane of G2 (Fig. 5a). Except for the shuffling accompanying the $(200)_1$-to-$(\bar{1}11)_2$ transformation, an additional shear with a magnitude of $\frac{\sqrt{2}}{4}a$ (indicated by the orange arrow, which is parallel to $\langle 0\bar{1}1\rangle_2$ direction and contributed by the screw component of $\boldsymbol{b}_1$ type disconnections), and shuffling (indicated by the green arrow) within the $(020)_1$ plane are needed to accomplish the $(020)_1$-to-$(200)_2$ lattice transformation (Fig. 5c). While for the type-2 GB migration, the motion of $\boldsymbol{b}_2$ type disconnection would lead to the transformation of $(020)_1$ atomic plane into the $(111)_2$ atomic plane (Fig. 5a), during which only atom shuffling is needed (Fig. 5c). Note that the dashed purple circles in Fig. 5c indicate the atoms in rearranged $(020)_1$ plane after the $(200)_1$-to-$(\bar{1}11)_2$ transformation, instead of the original $(020)_1$ plane. The crystallographic parameters of $\boldsymbol{b}_1$ type disconnections can thus be modified: the $\boldsymbol{b}_1$ type disconnection should have an edge component with the magnitude of $\frac{\sqrt{6}+2}{12}a$ and a screw component with the magnitude of $\frac{\sqrt{2}}{4}a$. Note that accurate crystallographic parameters of these GB disconnections can not be determined at this point mainly due to the uncertain extent of atoms shuffling.

3.4. MDs simulation of two types of GB migration

According to the theoretical analysis above, the GB disconnections in the two types of GB migration are deduced to have different crystallographic parameters and result in different lattice correspondence relations. Consequently, the activation of GB migration following different

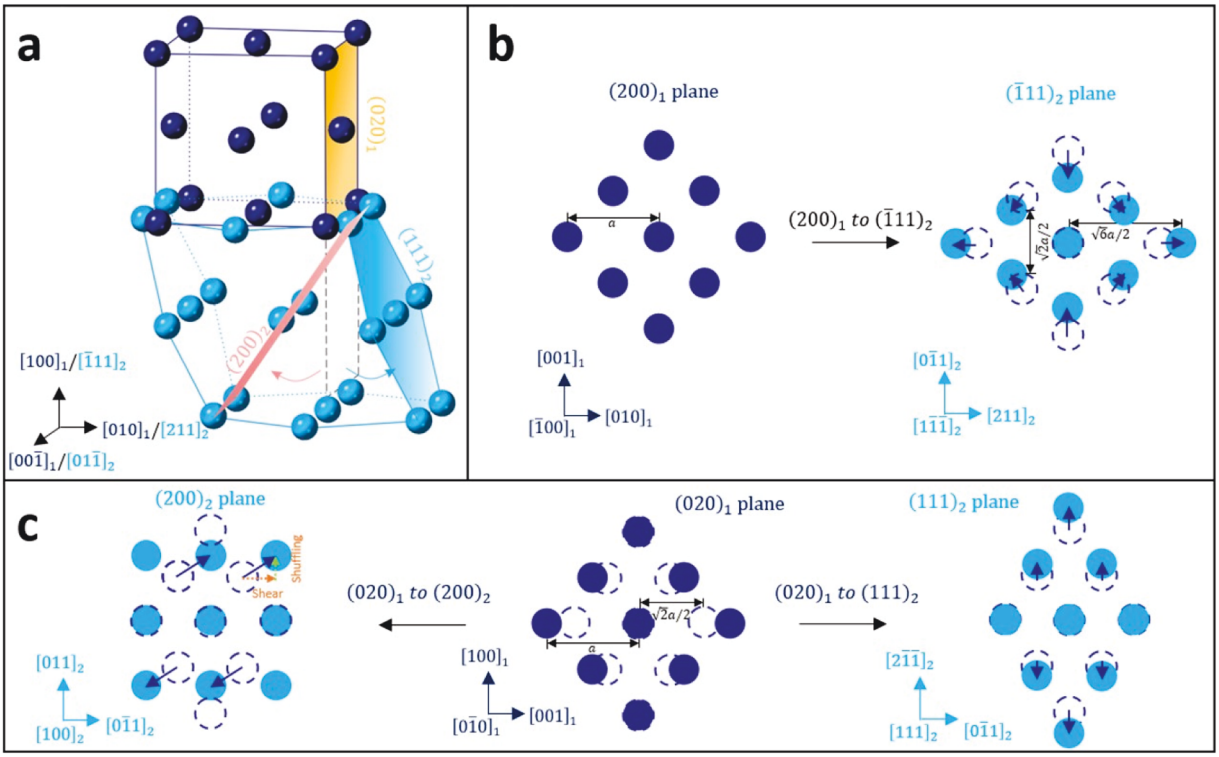

Fig. 5. Topological analysis of the lattice transformation relations during GB migration. (a) Atomic models of the $\langle 00\bar{1}\rangle$-oriented G1 and the $\langle 01\bar{1}\rangle$-oriented G2 with the (100) plane of G1 parrallel to the $(\bar{1}11)$ plane of G2. Atoms in G1 are colored purple while that in G2 are blue. (b) Schematic illustration showing the necessary localized atoms adjustment to complete the $(200)_1$-to- $(\bar{1}11)_2$ transformation. (c) Schematic illustration showing the two different lattice transformation relations: $(020)_1$-to-$(200)_2$ and $(020)_1$-to-$(111)_2$. The dash purple circles indicate the atoms arrangement of $(020)_1$ plane after the shuffling during the $(200)_1$-to- $(\bar{1}11)_2$ transformation. The purple arrows in (b) and (c) indicate the movement of atoms during the transformations. The dash orange arrow and the green arrow in (c) indicate the shear displacement contributed by the screw component of disconnection and the atoms shuffling to accompany the transformation, separately.

lattice correspondence relations would require different stress/strain states. Referring to the modified crystallographic parameters of the disconnections, the type-1 GB migration following the $(020)_1$-to-$(200)_2$ plane transformation (i.e., mediated by $\boldsymbol{b}_1$ type disconnection) is preferred when the shear loading has an angle around 43.6° with the $\langle 010\rangle_1$ direction, while the type-2 GB migration following the $(020)_1$-to-$(111)_2$ plane transformation is activated when the shear loading is parallel to the $\langle 010\rangle_1$ direction. Considering that HRTEM images are projective and phase-contrast images, exactly resolving the structure change along the beam direction and the lattice correspondence relations during GB migration from HRTEM images is difficult. Therefore, we constructed two MD simulation models, one has the shear direction parallel to the $\langle 010\rangle_1$ direction but the one has the shear direction parallel to the $\langle 0\bar{1}1\rangle_1$ direction, to further verify the two types of GB migration and underlying lattice correspondence relations.

Fig. 6 presents the case of shearing parallel to the $\langle 010\rangle_1$ direction. As shown in Fig. 6a and 6b, after the shear deformation, the original flat $(200)_1/(\bar{1}11)_2$ GB in the bicrystal was replaced by a twin boundary and an inclined GB consisting of $(200)/(\bar{1}11)$ GB nanofacets, which exactly matches the GB deformation behavior in Fig. 2e-f. The formation of the twin boundary is because that the shear direction $\langle 010\rangle_1$ is parallel to the Burgers vector of one of the Shockley partial dislocations of the bottom grain G2. Thereafter, an analysis of the sequential snapshots of MD simulations was performed to view the atomistic process of GB migration. From the analysis, we noticed that the GB deformation along the $[001]_1$ direction of the bicrystal is complicated and not uniform. To better elucidate this non-uniform GB deformation, the front views of the bicrystal at different depths along the $[001]_1$ direction during the deformation are presented in Fig. 6c-f (i.e., middle) and Fig. 6g-j (i.e., side), and meanwhile the top views of a selected $(200)_1$ atomic plane (indicate by the red arrows in Fig. 6c and 6g) during the deformation are shown in Fig. 6k-n. Note that Fig. 6c-f, 6 g-j, and 6k-n are taken at the same time sequence. In addition, several $(020)_1$ atomic planes are colored in orange to show the transformations of these atomic planes during GB migration (Fig. 6c-j).

At the incipient stage of deformation, there is a new grain (denoted as G3) that was formed at the region at the middle of the GB (Fig. 6k) and near the right side free surface of the bicrystal (Fig. 6c). The new grain G3 is in twinning relation with the bottom grain G2. While for the region near the front (and back) side of the bicrystal, the GB first migrated downward for several atomic layers through the collective motion of one-atomic-layer $\boldsymbol{b}_2$ type GB disconnections (Fig. 6g and 6k). Then, a new grain G4 that is also in a twinning relationship with G2 was formed (Fig. 6e and 6h) and the growth of G4 at subsequent deformation was via the collective migration of the $(200)_1/(\bar{1}11)_4$ GB nanofacets (Fig. 6h-j). The collective migration of these $(200)_1/(\bar{1}11)_4$ GB nanofacets exactly followed the (020)-to-(111) type lattice correspondence relation (i.e., type-2 GB migration), as directly evidenced by the transformation of the vertical $(020)_1$ atomic planes (colored in orange) into the inclined $(111)_4$ atomic planes (Fig. 6g-j). Back to the complex deformation at the middle-right region of GB, the new grain G3 did not grow like G4. Instead, the entire G3 glided along the $(200)_1/(\bar{1}11)_2$ GB, which was enabled by the motion of disconnections that are between G1 and G3. It requires that these disconnections (indicated by the solid and the dashed blue curves in Fig. 6m and 6n) have different Burgers vectors, i.e., $\boldsymbol{b}_2$ type and $\boldsymbol{b}_1$ type. In fact, stacking faults (SFs) were formed in G3 before the glide of G3 as a whole. The formation of SFs can exactly compensate for the differences in the screw component between $\boldsymbol{b}_1$ type and $\boldsymbol{b}_2$ type disconnections.

Fig. 7 shows the case of shearing parallel to the $\langle 0\bar{1}1\rangle_1$ direction. In

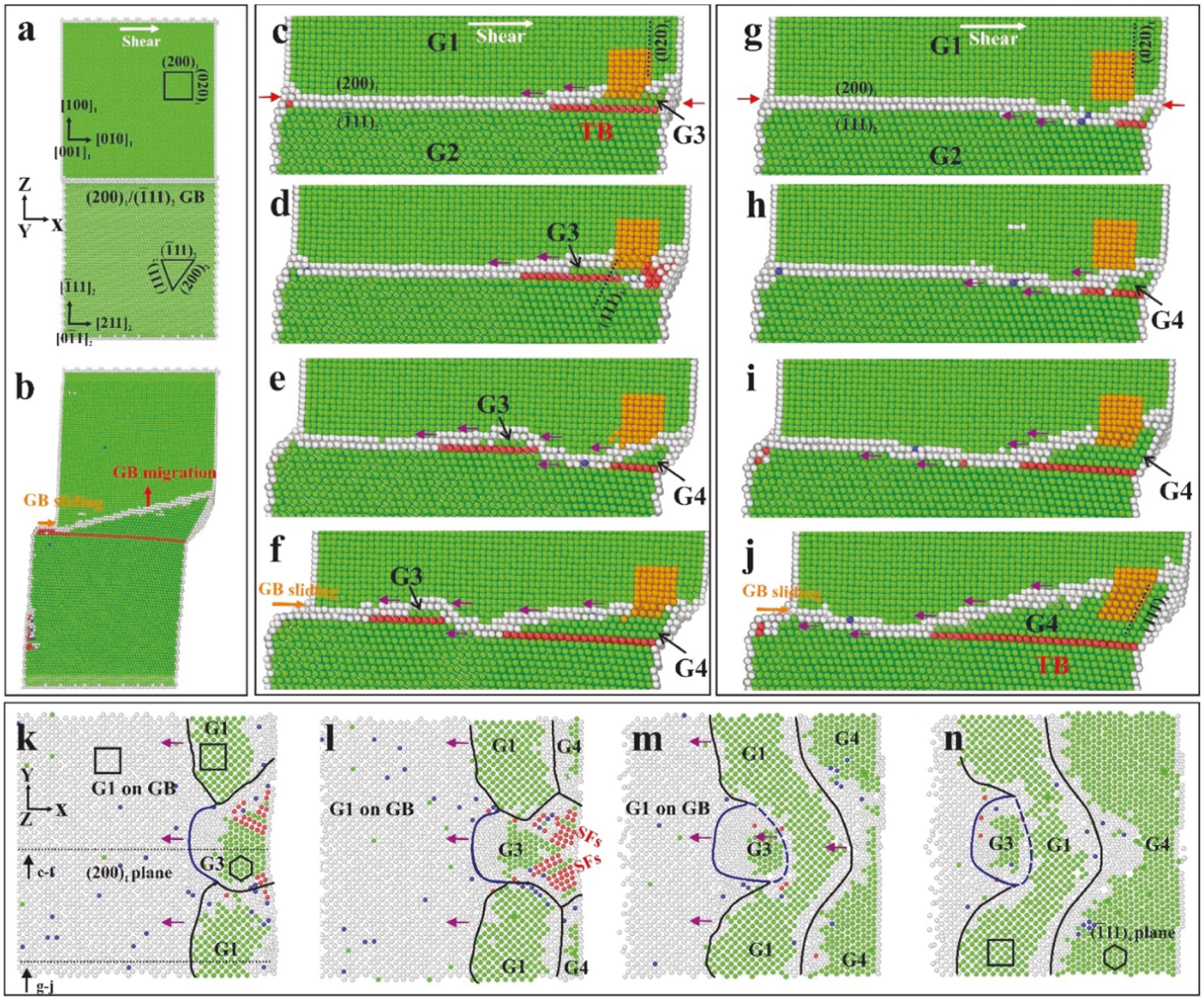

Fig. 6. MD results of GB migration following the $(020)_1$-to-$(111)_2$ type lattice transformation. (a, b) Au bicrystal before and after the shear deformation. Shear displacement was applied on the top fixed end along the $[010]_1$ direction. (c-f, g-j) Sequential snapshots showing the GB structures at different depths along the $[010]_1$ direction. The sliced positions are indicated by the dashed lines in k. Selected atom columns on $(020)_1$ atomic planes were colored orange to show the lattice transformation. New grains formed after twinning are denoted as G3 and G4, separately. The purple arrows indicate the motion directions of GB disconnections. (k-n) Top views of a thin (indicated by the red arrows in c and g) atomic layer showing the atomic plane transformation during GB migration in c-f and g-h. The curved lines represent the disconnection lines between different grains. Green atoms represent the bulk face-centered cubic atoms while white ones indicate boundary atoms.

this case, the bicrystal was rotated 45° around the $[100]_1$ direction to present the lattice transformation during GB migration (Fig. 7a). After shear deformation, the $(200)_1/(\bar{1}11)_2$ GB migrated downward (Fig. 7b). The sequential snapshots of MD simulations results in Fig. 7c-f show that the GB migration in this case followed the (020)-to-(200) type lattice correspondence relation (i.e., type-1 GB migration), as evidenced by the transformation of the inclined $(200)_2$ atomic planes (colored in dark green) into the vertical $(020)_1$ atomic planes. Meanwhile, the top views of the selected $(\bar{1}11)_2$ atomic plane (indicated by the red arrows in Fig. 7c) captured at the same time sequence as that of Fig. 7c-f clearly shows the $(\bar{1}11)_2$-to-$(200)_1$ plane transformation was mediated by the motion of GB disconnection (Fig. 7g-j).

The MD simulation results confirm the two different GB migration patterns and underlying lattice correspondence relations, i.e., (020)-to-(111) type and (020)-to-(200) type, of the $(200)_1/(\bar{1}11)_2$ GB. In addition, akin to experimental results in Fig. 2b-g, GB sliding and GB plane reorientation are found to concurrently occur with the GB migration (Fig. 6b and 7b). Notably, the GB sliding also happened on the $(200)_1$ / $(\bar{1}11)_2$ GB plane, as reflected in the surface steps that were formed after the shear deformation of the bicrystals (Figs. 6b and 7b).

3.5. Origin of excess GB sliding and GB plane reorientation

Given that both experimental (Fig. 2b-g) and simulational (Figs. 6 and 7) results indicate that excess GB sliding and GB plane reorientation accommodate the GB migration, additional theoretical analysis was performed to pinpoint the roots of these phenomena. In theory, GB migration is essentially the result of lattice transformation between the adjoining crystals [6,20]. Therefore, disconnection-mediated shear--coupled GB migration has to establish a point-to-point lattice correspondence relation between the crystals. For the symmetrical tilt GBs such as the Σ11(113) symmetrical tilt GB, the atomic planes perpendicular to the GB are identical, e.g., {113} planes, which makes the point-to-point lattice correspondence during GB migration easy to establish. In comparison, the non-symmetrical GBs such as asymmetrical tilt GBs and MGBs have different atomic planes adjoined at the GB plane. Different atomic planes have different planar packing fractions (PPFs), which makes the establishment of point-to-point lattice correspondence in non-symmetrical GBs more difficult than that in symmetrical tilt GBs. There must be some prerequisites for the GB disconnections so they can effectively mediate the shear-coupled migration of these non-symmetrical GBs. For instance, Pond et al. investigated the structure and mobility of various interfacial defects, i.e., disconnections, at a ⟨

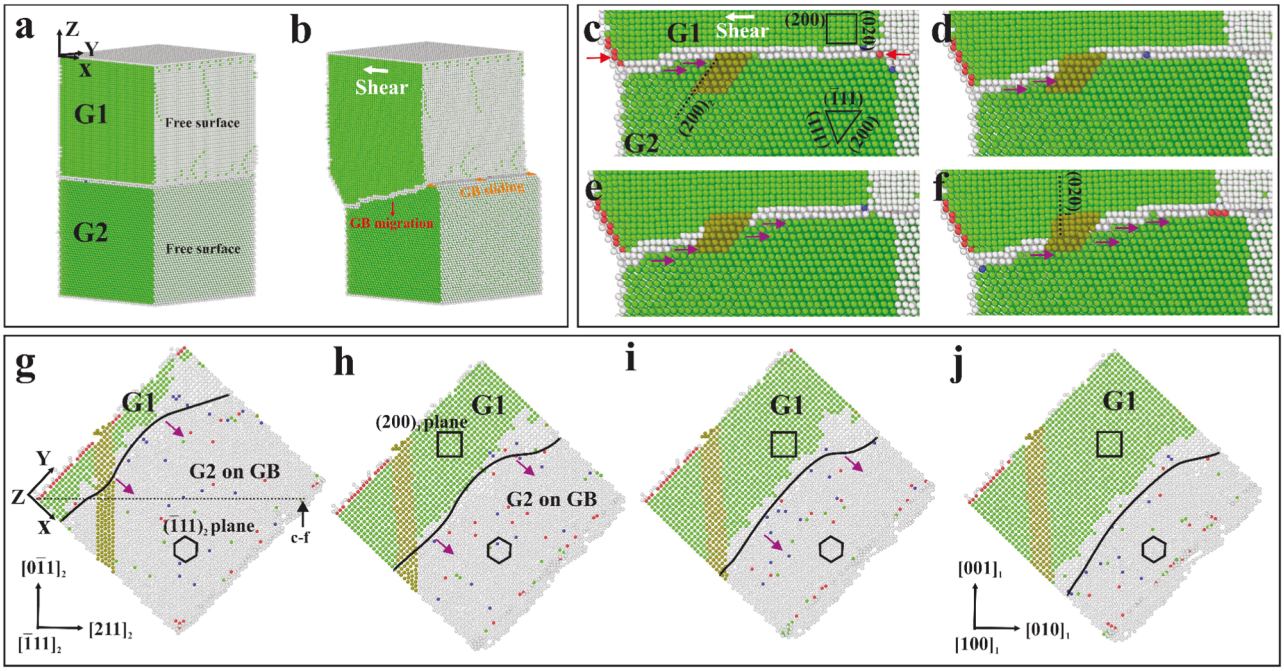

Fig. 7. MD results of GB migration following the $(200)_2$-to-$(020)_1$ lattice transformation. (a, b) Au bicrystal before and after the shear deformation. Shear displacement was applied on the top fixed end along the x-axis of the bicrystal, i.e., $[01\bar{1}]_1$ direction. (c-f) Sequential snapshots showing the $(200)_2$-to-$(020)_1$ lattice plane transformation during the GB migration. The sliced positions are indicated by the dashed lines in g. Atoms on $(200)_2$ atomic planes are selectively colored in dark green to trace the lattice transformation. The purple arrows indicate the motion directions of GB disconnections. (g-j) Top views of a thin slice perpendicular to the z-axis showing the $(\bar{1}11)_2$-to-$(200)_1$ atomic plane transformation during GB migration in c-f. The position of the thin slice is indicated by the red arrows in c.

110⟩ 90° (111)/(1$\bar{2}$1) asymmetrical tilt GB in Au using postmortem HRTEM and atomistic simulation, and they found that only the $\boldsymbol{b}_{3/1}$ disconnections (3/1 means three (2$\bar{4}$2) atomic planes match one (111) atomic plane at the disconnections) can move conservatively under an applied shear strain, as to ensure the constant total number of atoms during GB migration [22].

Regarding the ⟨001⟩{200}/⟨0$\bar{1}$1⟩{$\bar{1}$11} MGB in our work, our results have shown that the dominant GB disconnections mediating the GB migration have a step height of one atomic layer, i.e., one (200) atomic plane matches one ($\bar{1}$11) atomic plane at the disconnections (Fig. 3), and have $b_p = \frac{2\sqrt{3}-3}{6}a$. As presented in ref [45], when a disconnection of a length L and step height h moves in a velocity of v, the diffusive flux during the motion can be expressed as:

$$I = Lv\left[h\Delta X + b_p X\right] \tag{2}$$

where ΔX indicates the difference in the number of atoms per unit volume between the two crystals μ and λ, e.g., X^{λ}-X^{μ}; X could be either X^{λ} or X^{μ}, depending on the direction of disconnection movement; b_p is the disconnection's Burgers vector component that is perpendicular to the interface, i.e., the climb component. In the present case, crystals μ and λ are Au crystals having the identical number of atoms per unit volume (i.e., X^{λ}=X^{μ}), which makes $\Delta X = 0$. Then, Eq. (2) can be re-formulated as:

$$I = Lvb_p X \tag{3}$$

Therefore, the diffusive flux accompanying the motion of a disconnection is directly caused by the motion of the climb component of the disconnection, i.e. b_p. The diffusional flux of these one-atomic-layer disconnections is non-zero as $b_p = \frac{2\sqrt{3}-3}{6}a$, which suggests these disconnections cannot move conservatively. To further elaborate on this issue, we estimated the climbing velocity of these one-atomic-layer disconnections to explain the observed mobility of these disconnections. The estimation of climbing velocity (See Supplementary discussion for the calculation) was carried out using the method presented in Ref [21] and gave a value of 1.47 $\mu m\ s^{-1}$ which is higher by five orders of magnitude than the deformation speed applied in the experiments, i.e., 0.01 $nm\ s^{-1}$. Hence, it is believed that a high velocity of the moving climb component of these disconnections could result in the observed mobility of these disconnections.

As the motion of a one-atomic-layer disconnection alone cannot mediate the conservative migration of the MGB, excess GB sliding occurred simutaneously with GB migration. Moreover, to eventually achieve the conservative GB migration, the area ratio of the (200) and ($\bar{1}$11) planes matched at the GB has to be inversely proportional to the PPFs ratio of these planes ($PPF\{111\}/PPF\{002\} = 1.154$), ensuring the constant total number of atoms during GB migration. The GB plane reorientation can exactly alter the area ratio of the matching (200) and ($\bar{1}$11) planes at the GB and a simplified geometrical model is proposed as follows to elucidate it. Fig. 8b illustrates the scenario that the ⟨001⟩{200}/⟨0$\bar{1}$1⟩{$\bar{1}$11} MGB plane rotated anticlockwise around the out-of-paper direction by a certain angle α. Assuming the length of the bicrystal along the out-of-plane direction is a constant, the rotated GB plane would have the area ratio of the matching (200) and ($\bar{1}$11) planes equal to the length ratio of $l_{(200)1}$ and $l_{(\bar{1}11)2}$ as shown in Fig. 8b. The relations between $l_{(200)1}$, $l_{(\bar{1}11)2}$, and the length of the projected GB plane, i.e., l_{GB}, are as follows:

$$l_{(200)1} = l_{GB}\cos\alpha \tag{4}$$

and

$$l_{(\bar{1}11)2} = l_{GB}\sin(109.5^{\circ} - \alpha)/\sin\alpha \tag{5}$$

Then, the length ratio is

$$l_{(200)1}/l_{(\bar{1}11)2} = \sin\alpha\cos\alpha/\sin(109.5^{\circ} - \alpha) \tag{6}$$

On the basis of Eqn. (6), the change of length ratio to the inclination angle α is plotted in Fig. 8c. It clearly shows that the length ratio increases with the inclination angle, and equals the PPFs ratio of ($\bar{1}$11) and

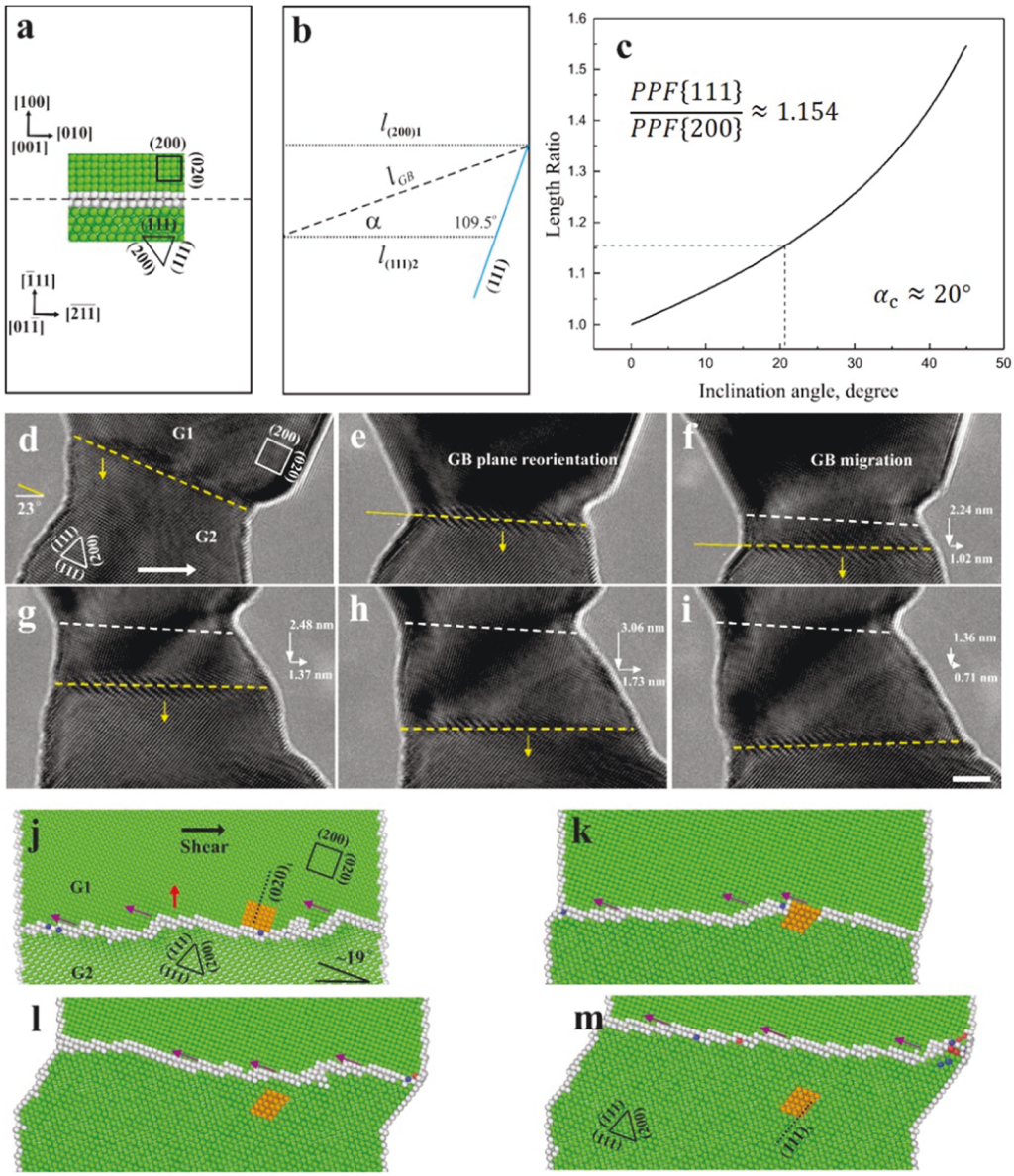

Fig. 8. Geometrical analysis of the concurrent GB migration and GB sliding under shear deformation. (a, b) Schematics of bicrystals with a flat $\langle 001\rangle\{200\}/\langle 0\bar{1}1\rangle\{\bar{1}11\}$ GB (a) and with the GB plane reoriented by a certain inclination angle α (b). The lengths of the atomic planes matching at the GB change with the reorientation of GB. (b) Plot of the length ratio between $(200)_1$ and $(111)_2$ planes that match at the reoriented GB plane. (d-i) Sequential HRTEM images showing the shear deformation of the Au bicrystal was dominated by GB migration after the GB plane reoriented to α = 23°. (j-m) MD simulation results showing the migration of a GB with α = 19° was accommodated by the coordinate migration of $\langle 001\rangle\{200\}/\langle 0\bar{1}1\rangle\{\bar{1}11\}$ GB facets. Scale bar. (d-i) 5 nm.

(200) planes at the inclination angle of ~20°. It indicates that GBs with an inclination angle close to 20° could build up the point-to-point lattice correspondence and thus migrate conservatively. To verify this conjecture, both experimental and simulational studies were performed and shown in Fig. 8d-m. Fig. 8d-i present the experimental results that an Au bicrystal with the $\langle 001\rangle_1\{200\}_1/\langle 0\bar{1}1\rangle_2\{111\}_2$ GB was deformed by the applied shear strain (indicated by the white arrow in Fig. 8d), where the shear direction has a rotated angle of ~23° to the original GB plane. At the incipient deformation stage, the GB plane is reoriented to be nearly parallel to the shear direction (Fig. 8e). Then, the re-oriented GB migrated with no further GB plane reorientation observed (Fig. 8f-i). The $\{\bar{1}11\}_2$ surface facet of the bottom grain clearly changed into the $\{020\}_1$ surface facet of the upper grain under the shear loading, which accompanied the GB migration towards the bottom grain. Additionally, the shear-coupling factor during the steady state of GB migration (Fig. 8f-i) is measured to be ~0.55±0.02, which reasonably matches the theoretical value of ~0.523 that is calculated based on the $\{\bar{1}11\}_2$-to-$\{020\}_1$ lattice correspondence relationship ($\beta \approx \tan 39^\circ - \tan 16^\circ$). In addition, Fig. 8j-m show the simulational results of the shear-coupled migration of a $\langle 001\rangle_1\{3\bar{1}0\}_1/\langle 0\bar{1}1\rangle_2\{255\}_2$ GB that has an inclination angle of ~19° to the $\langle 001\rangle_1\{200\}_1/\langle 0\bar{1}1\rangle_2\{111\}_2$ GB. The as-constructed $\langle 001\rangle_1\{3\bar{1}0\}_1/\langle 0\bar{1}1\rangle_2\{255\}_2$ GB had a faceted GB structure (Fig. 8j) that later transformed into an array of $\langle 001\rangle_1\{200\}_1/\langle 0\bar{1}1\rangle_2\{111\}_2$ GB nanofacets connected by the GB disconnections during the subsequent shear deformation (Fig. 8k-m). No substantial excess GB sliding and GB plane reorientation were observed during this process and the changes in the selected $(020)_1$ atomic planes (colored in orange) after the GB migration (Fig. 8m) proves the GB migration followed the $\{020\}_1$-to-$\{\bar{1}11\}_2$ lattice correspondence relationship.

It needs to mention that Fig. 8 only depicts the case of GB migration following the $\{020\}_1$-to-$\{\bar{1}11\}_2$ type lattice correspondence relationship (i.e., type-2 GB migration) as an example. GB migration following the $\{020\}_1$-to-$\{200\}_2$ type lattice correspondence relationship (i.e., type-1 GB migration) is also expected to reorient the GB plane to achieve the conservative GB migration (e.g., Fig. 1b-d), but such GB plane reorientation should not only occur around the out-of-plane direction (i.e., $[001]_1$) as that in Fig. 8 but occur around $[010]_1$direction since the GB disconnections mediating the $\{020\}_1$-to-$\{200\}_2$ type lattice transformation shall have an additional shear component parallel to the $[010]_1$direction. More delicate experimental or simulational studies are

needed in the future to elucidate the exact criteria of conservative GB migration following $\{020\}_1$-to-$\{200\}_2$ type lattice correspondence relation.

4. Discussion

MGBs have both tilt and twist components. A low-angle MGB is normally described as an array of edge and screw dislocations. The collective motion of these constituent dislocations accommodates the deformation of the low-angle MGB, wherein the edge dislocations contribute to GB migration whereas the screw ones cause grain rotation [19]. For the high-angle MGBs, previous simulation studies indicate that some special coincidence site lattice (CSL) MGBs, i.e., Σ3 [111] 60° boundary with {11 8 5} GB plane [46] and Σ7 [111] 38.21° MGBs [30], are faceted, stepped, or kinked at the atomic scale with the corresponding low-energy CSL symmetrical tilt GBs being the constituent GB facets or terraces. Based on the assumption that only the symmetrical tilt GB component contributes to the shear-coupled migration of MGBs, Han et al. [20] proposed an unverified theoretical equation to predict the shear-coupling factors of MGBs. However, CSL MGBs only represent a special set of GBs. MGBs in reality are generally the non-CSL GBs with irrational GB planes [47–49]. In these general cases, the MGBs normally consist of low-energy GB facets comprised of at least one low-index plane, e.g., (100), (110), and (111) planes, instead of symmetrical tilt GB facets. Our work takes the $\langle 001\rangle\{200\}/\langle 0\bar{1}1\rangle\{\bar{1}11\}$ MGB as an case study to uncover the atomistic mechanims of the shear-coupled migration of the MGBs comprised of at least one low-index plane, and our results provide the atomic-scale experimental evidence that the migration of MGBs could be mediated by the motion of GB disconnections on the MGB plane itself instead of on its symmetrical tilt GB component.

As shown in our results, there are several striking features of the shear-coupled migration of MGBs. First, there exist distinct types of migration behavior showing the opposite signs of shear-coupling factors for the same $\langle 001\rangle\{200\}/\langle 0\bar{1}1\rangle\{\bar{1}11\}$ MGB deformed at room temperature, which arises from the activation of GB disconnections with different crystallographic parameters (Fig. 3 and Table 1). As predicted by the disconnection theory, there is a broad spectrum of admissable GB disconnections with various choices of Burgers vectors and step heights for an arbitrary GB crystallography (including the symmetrical tilt GBs) [41,50,51]. Although GB disconnections with different Burgers vectors and step heights for the same GB have also been observed in the migration of some symmetrical tilt GBs, these disconnections either belong to the same type with the identical shear-coupling factors [12, 14] or produce the opposite signs of shear-coupling factors but can only be activated at different temperatures [52,53]. They are notably different from the two types of GB disconnections in MGBs that produce the opposite signs of shear-coupling factors at room temperature (Fig. 1). Secondly, the revealed two lattice correspondence relationships, i.e., (020)-to-(111) type and (020)-to-(200) type, during the shear-coupled migration of $\langle 001\rangle_1\{200\}_1/\langle 0\bar{1}1\rangle_2\{\bar{1}11\}_2$ MGB involves the transformations between different atomic planes, which are different from what happens in symmetrical tilt GBs wherein the corresponding planes are normally identical atomic planes. For instance, shear-coupled migration of $\langle 001\rangle$ tilt GBs involves the transformation of either {100} or {110} atomic planes of one lattice into the identical atomic planes of the other lattice, depending on the misorientation angle and the deformation temperature [6,13]. Instead, they are similar to the Basal-Prismatic [54,55] and Basal-Pyramidal [56,57] transformations that have been extensively studied in hexagonal-close packed metals that commonly involve complex atoms shuffling. Thirdly, the unique transformation relations between different atomic planes during GB migration bring the results that the $\langle 001\rangle\{200\}/\langle 0\bar{1}1\rangle\{\bar{1}11\}$ MGB cannot easily migrate conservatively like the symmetrical tilt GBs. GB plane reorientation and excess GB sliding shall be activated to accommdate the GB migration. The GB plane reorientation occurred via the stack of $\langle 001\rangle\{200\}/\langle 0\bar{1}1\rangle\{\bar{1}11\}$ GB nanofacets that migrated at different distances, regardless of which lattice correspondence relation the GB migration follows (Figs. 1e-g, 6, and 7). Note that the GB plane reorientation is also found to occur during the shear-coupled migration of asymmetrical tilt GBs as reported in our recent work [29]. The excess GB sliding can be mediated by the motion of GB disconnections that have Burgers vectors but no step height [20,58].

Admittedly, the free surface of the nano-bicrystals plays important role in accommodating the GB migration in our cases. First, the intersection of free surface with the GB serves as the primary nucleation site for the GB disconnections (Fig. 2). Secondly, the sample geometry (i.e., the large taper angle of free surface with the GB) could also propel the nucleation of GB disconnections or the twin [59]. In comparison, GB migration in nanocrystalline materials receives constraints from the neighboring grains. The nucleation of GB disconnections in nanocrystalline materials could either be via the homogeneous/heterogeneous nucleation of disconnection pairs [23], or occur at the GB triple-junctions [60], but not at the free surface in our case. Moreover, GB migration in nanocrystalline materials is commonly accommodated by GB junctions, the motion of which requires the net Burgers vector of disconnections into/out of the junctions to be zero [61–63]. Otherwise, other deformation mechanisms such as the emission of lattice dislocations or the twinning would be activated to dissipate the accumulated Burgers vectors [61,64]. Therefore, shear-coupled GB migration in nanocrystalline materials depends largely on the local environment of the GB. For the typical case of $\langle 001\rangle_1\{200\}_1/\langle 0\bar{1}1\rangle_2\{\bar{1}11\}_2$ MGB studied here, there are multiple admissible combinations of active deformation modes in the polycrystalline environment: type-1 shear-coupled GB migration and excess GB sliding (Figs. 1b-d, Fig. 7); type-2 shear--coupled GB migration and excess GB sliding (Fig. 6); and the concurrent type-1 and type-2 shear-coupled GB migration (Fig. 1e-g). Note that cooperative GB sliding and GB migration have also been observed in the tensile deformation of an Au nanocrystalline thin film [65]. An example of MGB migration mediated by the GB triple-junction can be found in Supplementary Fig. 2. Moreover, akin to the twinning-assisted dynamic adjustment of GB mobility during the shear-coupled migration of $\langle 110\rangle$ tilt GBs [66], twinning is also found to assist the transition between the two migration modes of the $\langle 001\rangle_1\{200\}_1/\langle 0\bar{1}1\rangle_2\{\bar{1}11\}_2$ type MGB (Supplementary Fig. 3). Lastly, it is worth mentioning that temperature [52,67], shear direction [58], and strain rate [68] could also affect the shear-coupled migration behavior of GBs. It is expected that other migration modes can be observed when these factors are varied, which undoubtedly warrant attention in future study.

5. Conclusion

By conducting in situ HRTEM shear testing and MD simulations, we have explored the shear-coupled migration behavior and underlying atomistic mechanisms of a typical MGB, i.e., $\langle 001\rangle_1\{200\}_1/\langle 0\bar{1}1\rangle_2\{\bar{1}11\}_2$ GB, in Au nanocrystals. The main conclusions are summarized as follows:

1) Two distinct types of shear-coupled GB migration behavior having the opposite signs of shear-coupling factors were observed at the room-temperature shear deformation of the $\langle 001\rangle_1\{200\}_1/\langle 0\bar{1}1\rangle_2\{\bar{1}11\}_2$ MGB. Both migration patterns can be mediated by the motion of one-atomic-layer GB disconnections on the MGB plane, but these disconnections have different Burgers vectors.
2) Based on topological analysis of the crystallographic parameter of these GB disconnections, two completely different lattice correspondence relations, i.e., $\langle 001\rangle\{020\}$-to-$\langle 0\bar{1}1\rangle\{200\}$ type and $\langle 001\rangle\{020\}$-to-$\langle 0\bar{1}1\rangle\{111\}$ type, during the MGB migration, were proposed and then verified by the MD simulations. Except for the

shear displacement of atoms, complex atom shuffling is needed in both cases to complete the lattice transformation.

3) GB plane reorientation and excess GB sliding were observed to accommodate the shear-coupled migration of the MGB regardless of which lattice correspondence relation it follows. A simplified geometrical model, derived from the principle of point-to-point lattice correspondence during GB migration, is proposed to account for the necessity of these extra mechanisms to eventually achieve the conservative migration of this MGB.
4) Our findings not only provide direct experimental evidence on the disconnection-mediated migration of MGBs and the atomistic understanding of the lattice transformation during the migration of MGBs, but also show that the shear response of MGBs is much more complex than that of symmetrical tilt GBs in a way that multiple deformation mechanisms, e.g., different shear-coupled migration modes, GB plane reorientation, and excess GB sliding, could be cooperatively activated. Given that MGBs comprised of at least one low-index plane wildly exist in face-centered cubic polycrystals, the observed phenomena and uncovered mechanisms should have general implications for a wide range of GBs and may provide guidance for tailoring the mechanical properties of nanocrystalline materials through GB engineering.

Declaration of Competing Interest

The authors declare that they have no known competing financial interests or personal relationships that could have appeared to influence the work reported in this paper.

Acknowledgments

G. W. acknowledges support from National Science Foundation (NSF DMR 1808046) through the University of Pittsburgh. This research was supported in part by the University of Pittsburgh Center for Research Computing through the resources provided. Specifically, this work used the H2P cluster, which is supported by NSF award number OAC-2117681.

Supplementary materials

Supplementary material associated with this article can be found, in the online version, at doi:10.1016/j.actamat.2023.119237.

References

[1] J. Hu, et al., Grain boundary stability governs hardening and softening in extremely fine nanograined metals, Science 355 (6331) (2017) 1292–1296.
[2] T.J. Rupert, et al., Experimental observations of stress-driven grain boundary migration, Science 326 (5960) (2009) 1686–1690.
[3] F. Mompiou, D. Caillard, M. Legros, Grain boundary shear–migration coupling—I. In situ TEM straining experiments in Al polycrystals, Acta Mater. 57 (7) (2009) 2198–2209.
[4] J.P. Liebig, et al., Grain boundary mediated plasticity: a blessing for the ductility of metallic thin films? Acta Mater. 215 (2021), 117079.
[5] B.B. Zhang, et al., Inhibiting creep in nanograined alloys with stable grain boundary networks, Science 378 (6620) (2022) 659–663.
[6] J.W. Cahn, Y. Mishin, A. Suzuki, Coupling grain boundary motion to shear deformation, Acta Mater. 54 (19) (2006) 4953–4975.
[7] J.W. Cahn, J.E. Taylor, A unified approach to motion of grain boundaries, relative tangential translation along grain boundaries, and grain rotation, Acta Mater. 52 (16) (2004) 4887–4898.
[8] T. Gorkaya, D.A. Molodov, G. Gottstein, Stress-driven migration of symmetrical ⟨100⟩ tilt grain boundaries in Al bicrystals, Acta Mater. 57 (18) (2009) 5396–5405.
[9] J.-E. Brandenburg, D.A. Molodov, On shear coupled migration of low angle grain boundaries, Scr Mater 163 (2019) 96–100.
[10] D.A. Molodov, T. Gorkaya, G. Gottstein, Migration of the Σ7 tilt grain boundary in Al under an applied external stress, Scr. Mater. 65 (11) (2011) 990–993.
[11] D.A. Molodov, V.A. Ivanov, G. Gottstein, Low angle tilt boundary migration coupled to shear deformation, Acta Mater. 55 (5) (2007) 1843–1848.
[12] Q. Zhu, et al., In situ atomistic observation of disconnection-mediated grain boundary migration, Nat. Commun. 10 (1) (2019) 156.
[13] B. Li, J. Leung, Lattice transformation in grain boundary migration via shear coupling and transition to sliding in face-centered-cubic copper, Acta Mater. 215 (2021), 117127.
[14] L. Zhang, et al., Shear response of copper Bicrystal with ∑11 symmetric and asymmetric tilt grain boundaries by molecular dynamics simulation, Nanoscale 7 (2015).
[15] F. Mompiou, M. Legros, D. Caillard, SMIG model: a new geometrical model to quantify grain boundary-based plasticity, Acta Mater. 58 (10) (2010) 3676–3689.
[16] D. Caillard, F. Mompiou, M. Legros, Grain-boundary shear-migration coupling. II. Geometrical model for general boundaries, Acta Mater. 57 (8) (2009) 2390–2402.
[17] K.D. Molodov, D.A. Molodov, Grain boundary mediated plasticity: on the evaluation of grain boundary migration - shear coupling, Acta Mater. 153 (2018) 336–353.
[18] V. Randle, et al., Five-parameter grain boundary distribution of commercially grain boundary engineered nickel and copper, Acta Mater. 56 (10) (2008) 2363–2373.
[19] T. Gorkaya, et al., Concurrent grain boundary motion and grain rotation under an applied stress, Acta Mater. 59 (14) (2011) 5674–5680.
[20] J. Han, S.L. Thomas, D.J. Srolovitz, Grain-boundary kinetics: a unified approach, Prog Mater Sci 98 (2018) 386–476.
[21] A. Rajabzadeh, et al., The role of disconnections in deformation-coupled grain boundary migration, Acta Mater. 77 (2014) 223–235.
[22] D.L. Medlin, D. Cohen, R.C. Pond, Accommodation of coherency strain by interfacial disconnections at a 90° ⟨110⟩ grain boundary in gold, Philos. Mag. Lett. 83 (4) (2003) 223–232.
[23] N. Combe, F. Mompiou, M. Legros, Heterogeneous disconnection nucleation mechanisms during grain boundary migration, Phys. Rev. Mater. 3 (6) (2019).
[24] Combe, N., F. Mompiou, and M.J.P.R.B. Legros, Disconnections kinks and competing modes in shear-coupled grain boundary migration. 2016. 93(2): p. 024109.
[25] A. Rajabzadeh, et al., Elementary mechanisms of shear-coupled grain boundary migration, Phys. Rev. Lett. 110 (26) (2013), 265507.
[26] H.A. Khater, et al., The disconnection mechanism of coupled migration and shear at grain boundaries, Acta Mater. 60 (5) (2012) 2007–2020.
[27] L. Wang, et al., Tracking the sliding of grain boundaries at the atomic scale, Science 375 (6586) (2022) 1261–1265.
[28] L. Wan, J. Li, Shear responses of -tilt {1 1 5}/{1 1 1} asymmetric tilt grain boundaries in fcc metals by atomistic simulations, Modell. Simul. Mater. Sci. Eng. 21 (5) (2013), 055013.
[29] Z. Fang, et al., Atomic-scale observation of dynamic grain boundary structural transformation during shear-mediated migration, Sci. Adv. 8 (45) (2022) eabn3785.
[30] R. Hadian, et al., Atomistic migration mechanisms of atomically flat, stepped, and kinked grain boundaries, Phys. Rev. B 94 (16) (2016).
[31] S. Plimpton, Fast parallel algorithms for short-range molecular dynamics, J. Comput. Phys. 117 (1) (1995) 1–19.
[32] G. Grochola, S.P. Russo, I.K. Snook, On fitting a gold embedded atom method potential using the force matching method, J. Chem. Phys. 123 (20) (2005), 204719.
[33] A. Gautam, et al., Atomic structure characterization of an incommensurate grain boundary, Acta Mater. 61 (13) (2013) 5078–5086.
[34] F. Lancon, et al., Superglide at an internal incommensurate boundary, Nano Lett. 10 (2) (2010) 695–700.
[35] J.A. Brown, Y. Mishin, Dissociation and faceting of asymmetrical tilt grain boundaries: molecular dynamics simulations of copper, Phys. Rev. B 76 (13) (2007).
[36] A. Stukowski, Visualization and analysis of atomistic simulation data with OVITO–the open visualization tool, Modell. Simul. Mater. Sci. Eng. 18 (1) (2009), 015012.
[37] K.L. Merkle, D. Wolf, Quasiperiodic features in the atomic structure of long-period grain boundaries, Mater. Lett. 17 (5) (1993) 217–222.
[38] P.A. Deymier, M. Shamsuzzoha, J.D. Weinberg, Experimental evidence for a structural unit model of quasiperiodic grain boundaries in aluminum, J. Mater. Res. 6 (7) (1991) 1461–1468.
[39] X. Sun, et al., Dislocation-induced stop-and-go kinetics of interfacial transformations, Nature 607 (7920) (2022) 708–713.
[40] Q. Zhu, et al., Metallic nanocrystals with low angle grain boundary for controllable plastic reversibility, Nat. Commun. 11 (1) (2020) 3100.
[41] R.C. Pond, J.P. Hirth, Defects at surfaces and interfaces, in: H. Ehrenreich, D. Turnbull (Eds.), Solid State Physics, Academic Press, 1994, pp. 287–365. Editors.
[42] R. Pond, D. Vlachavas, Bicrystallography, Proc. R. Soc. Lond.. A. Math. Phys. Sci. 386 (1790) (1983) 95–143.
[43] J.P. Hirth, R.C. Pond, Compatibility and accommodation in displacive phase transformations, Prog. Mater. Sci. 56 (6) (2011) 586–636.
[44] R.C. Pond, D.L. Medlin, A. Serra, A study of the accommodation of coherency strain by interfacial defects at a grain boundary in gold, Philos. Mag. 86 (29–31) (2006) 4667–4684.
[45] Hirth, J. and R.J.A.M. Pond, Steps, dislocations and disconnections as interface defects relating to structure and phase transformations. 1996. 44(12): p. 4749–4763.
[46] J. Humberson, E.A. Holm, Anti-thermal mobility in the Σ3 [111]60° {11 8 5} grain boundary in nickel: mechanism and computational considerations, Scr. Mater. 130 (2017) 1–6.
[47] V. Randle, Overview No. 127The role of the grain boundary plane in cubic polycrystals, Acta Mater. 46 (5) (1998) 1459–1480.

[48] K.L. Merkle, L.J. Thompson, F. Phillipp, In-Situ HREM studies of grain boundary migration, Interf. Sci., 12 (2) (2004) 277–292.
[49] Y. Guo, et al., In situ observation of atomic-scale processes accomplishing grain rotation at mixed grain boundaries, Acta Mater. 241 (2022), 118386.
[50] J.P. Hirth, J. Wang, C.N. Tomé, Disconnections and other defects associated with twin interfaces, Prog. Mater. Sci. 83 (2016) 417–471.
[51] J.P. Hirth, Dislocations, steps and disconnections at interfaces, J. Phys. Chem. Solids 55 (10) (1994) 985–989.
[52] T. Frolov, Effect of interfacial structural phase transitions on the coupled motion of grain boundaries: a molecular dynamics study, Appl. Phys. Lett. 104 (21) (2014), 211905.
[53] N. Combe, F. Mompiou, M. Legros, Disconnections kinks and competing modes in shear-coupled grain boundary migration, Phys. Rev. B 93 (2) (2016), 024109.
[54] B.Y. Liu, et al., Twinning-like lattice reorientation without a crystallographic twinning plane, Nat. Commun. 5 (2014) 3297.
[55] Y. He, et al., Direct observation of dual-step twinning nucleation in hexagonal close-packed crystals, Nat. Commun. 11 (1) (2020) 2483.
[56] B.-Y. Liu, et al., Rejuvenation of plasticity via deformation graining in magnesium, Nat. Commun. 13 (1) (2022) 1060.
[57] Z. Kou, et al., In situ atomic-scale observation of a novel lattice reorienting process in pure Ti, Scr. Mater. 166 (2019) 144–148.
[58] A. Hua, J. Zhao, Shear direction induced transition mechanism from grain boundary migration to sliding in a cylindrical copper bicrystal, Int. J. Plastic. 156 (2022), 103370.
[59] Q. Zhu, et al., Revealing extreme twin-boundary shear deformability in metallic nanocrystals, Sci. Adv. 7 (36) (2021) eabe4758.
[60] A. Rajabzadeh, et al., Evidence of grain boundary dislocation step motion associated to shear-coupled grain boundary migration, Philos. Mag. 93 (10–12) (2013) 1299–1316.
[61] S.L. Thomas, et al., Disconnection description of triple-junction motion, Proc. Natl. Acad. Sci. U.S.A., 116 (18) (2019) 8756–8765.
[62] M. Aramfard, C. Deng, Influences of triple junctions on stress-assisted grain boundary motion in nanocrystalline materials, Modell. Simul. Mater. Sci. Eng. 22 (5) (2014), 055012.
[63] L. Zhang, et al., Equation of motion for a grain boundary, Phys. Rev. Lett. 119 (24) (2017), 246101.
[64] H. Van Swygenhoven, P.M. Derlet, A. Hasnaoui, Atomic mechanism for dislocation emission from nanosized grain boundaries, Phys. Rev. B 66 (2) (2002), 024101.
[65] Q. Li, et al., In-situ observation of cooperative grain boundary sliding and migration in the nano-twinned nanocrystalline-Au thin-films, Scr. Mater. 180 (2020) 97–102.
[66] Q. Huang, et al., Twinning-assisted dynamic adjustment of grain boundary mobility, Nat. Commun. 12 (1) (2021) 6695.
[67] S.J. Fensin, M. Asta, R.G. Hoagland, Temperature dependence of the structure and shear response of a Σ11 asymmetric tilt grain boundary in copper from molecular-dynamics, Philos. Mag. 92 (34) (2012) 4320–4333.
[68] K. Chen, et al., Grain boundary shear coupling is not a grain boundary property, Acta Mater. 167 (2019) 241–247.